In-plane antiferromagnetic moments and magnetic polaron in the axion topological insulator candidate EuIn$_2$As$_2$

Yang Zhang [1,*] Ke Deng,[2,*] Xiao Zhang,[1] Meng Wang [1] Yuan Wang [2] Cai Liu [2] Jia-Wei Mei,[2] Shiv Kumar,[3]
Eike F. Schwier,[3] Kenya Shimada [3] Chaoyu Chen [2,†] and Bing Shen[1,‡]

[1]*School of Physics, Sun Yat-Sen University, Guangzhou, Guangdong 510275, China*
[2]*Shenzhen Institute for Quantum Science and Engineering (SIQSE), Southern University of Science and Technology, Shenzhen 518055, China*
[3]*Hiroshima Synchrotron Radiation Center, Hiroshima University, Higashihiroshima, Hiroshima 739-0046, Japan*

Topological insulator with antiferromagnetic order can serve as an ideal platform to realize axion electrodynamics. In this paper, we report a systematic study of the axion topological insulator candidate EuIn$_2$As$_2$. A linear energy dispersion across the Fermi level reveals a hole-type Fermi pocket. The orientation of the magnetic moment for ground state is determined within the *ab*-plane by anisotropic magnetic behavior. Besides long-range antiferromagnetic order, magnetization and magnetotransport measurements indicate existence of the ferromagnetic orders and ferromagnetic correlation, suggesting the formation of the magnetic polarons. These ferromagnetic clusters can persist above the antiferromagnetic transition leading to unconventional transport properties. Our results suggest multiple magnetic orders and states in EuIn$_2$As$_2$, which is vital to understanding its topological nature.

I. INTRODUCTION

Axion topological insulator (ATI) is an exotic material which can host hypothetic quasiparticles axions within the standard model of particle physics [1,2]. Axion electrodynamics emerge on the surface of topological insulators with magnetic order. It can be described by the formula

$$S_\theta = \frac{\theta e^2}{4\pi^2} \int \mathbf{E} \cdot \mathbf{B} \, dt \, d^3\mathbf{x}, \qquad (1)$$

where $\mathbf{E}$ and $\mathbf{B}$ are electromagnetic fields and the axion angle $\theta = \pi$ gives rise to the topological magnetoelectric (TME) effect [1,3]. The ATI is predicted to realize in intrinsic materials with antiferromagnetic (AF) order spontaneously breaking the time-reversal symmetry (TRS) [4–9], such as MnBi$_2$Te$_4$ [6]. The material with the intrinsic *A*-type AF order [10] hosts quantum anomalous Hall effect (QAHE) with a nonzero Chern number in the ultrathin flakes or films driven by a moderate magnetic field, which favors the former prediction of ATI [11–14]. Nonetheless, the observed short-range magnetic order associated with strong magnetic fluctuations [15] and the gapless Dirac surface state [16–21] indicate that the magnetic surface configuration and the topological states in MnBi$_2$Te$_4$ need to be treated carefully.

Different from layered van der Waals MnBi$_2$Te$_4$, EuIn$_2$As$_2$ exhibits a three-dimensional structure and crystallizes in the $P6(3)/mmc$ space group as shown in Fig. 1(a) [22]. It is an AF topological insulator candidate with tunable higher-order topological insulating states (HOTIS) and axion topological insulating states (ATIS) [8]. Particularly, the nontrivial topological states are strongly influenced by the detailed magnetization according to the theoretical calculations. Although the predicted magnetic order of the ground state is AF along the c axis for EuIn$_2$As$_2$, manipulating the direction of magnetic moments allows for achieving different topological states: in-plane magnetic moments (type A) result in an ATIS with gapped surface states while the out-of-plane magnetic moments (type B) lead to a HOTIS with hinge state on the domain wall of two gapped surfaces. Thus it is necessary to investigate the detailed magnetization (especially for the magnetic moment direction) for EuIn$_2$As$_2$ to pursue the insight of its topological nature. In this paper, we systematically study EuIn$_2$As$_2$ by combining angle resolved photoemission spectroscopy (ARPES) measurements and transport measurements. The in-plane magnetic moments of the AF ground state are revealed by anisotropic magnetic properties in accordance with the predicted type-A magnetic structure. The ARPES measurements reveal the hole-type Fermi surface made up of a linearly dispersing band, indicating that pristine EuIn$_2$As$_2$ is a metal instead of an insulator. More interestingly, the transport and magnetization measurements suggest ferromagnetic (FM) orders exist over the AF background and can even persist above the AF transition. We attribute these FM orders to the presence of the magnetic polaron (MP), which can strongly affect the transport properties as well as the topological nature.

II. EXPERIMENTAL DETAIL

Single crystals of EuIn$_2$As$_2$ were grown via the self-flux method. Eu, In, and As were mixed by the ratio of 1:10:2 and sealed inside an evacuated quartz tube. The mixture was heated to $1000\,^\circ$C, slowly cooled to $700\,^\circ$C, and finally decanted by a centrifuge. Planar single crystals with typical

*These authors contributed equally.
†Corresponding author: chency@sustech.edu.cn
‡Corresponding author: shenbingdy@mail.sysu.edu.cn
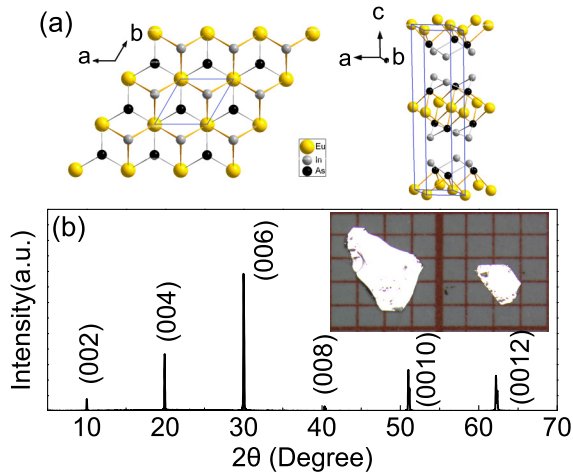
FIG. 1. (a) Crystal structure of $EuIn_2As_2$. (b) X-ray diffraction pattern of a single crystaline $EuIn_2As_2$. Perfect crystallinity is indicated by the set of (00l) peaks. Inset: picture of typical single crystals of $EuIn_2As_2$.

TABLE I. Crystal data and structure refinement for $EuIn_2As_2$ at 150 K.

Empirical formula	$EuIn_2As_2$
Formula weight	531.44
Crystal system	Hexagonal
Space group	$P63/mmc$
Unit cell dimensions	$a = 4.2068(5)$ Å
	$b = 4.2068(5)$ Å
	$c = 17.849(3)$ Å
α	$90°$
β	$90°$
γ	$120°$
Volume	$273.55(8)$ Å^3
Z	2
ρ(calc)	6.452 g/cm^3
μ	31.511 mm^{-1}
$F(000)$	454.0
Radiation	$MoK\alpha$ ($\lambda = 0.71073$)
2θ range for data collection	$9.136°$ to $69.908°$
Index ranges	$6 \leqslant h \leqslant 6$,
	$-5 \leqslant k \leqslant 3$,
	$-20 \leqslant l \leqslant 28$
Independent reflections	271 [$R_{int} = 0.0462$,
	$R_\sigma = 0.0443$]
Data/restraints/parameters	271/0/10
Goodness of fit on F^2	1.023
Final R indexes [$I \geqslant 2\sigma(I)$]	$R_1 = 0.0315$,
	$\omega R_2 = 0.0741$
Final R indexes [all data]	$R_1 = 0.0434$,
	$\omega R_2 = 0.0784$
Largest diff. peak/hole (e Å^3)	$1.63/-1.87$

dimensions of $2 \times 3 \times 0.3$ mm^3 were harvested as shown in the inset of Fig. 1(b). Crystal structure and elemental composition were confirmed by x-ray diffraction (XRD) and energy dispersive spectrometer (EDS). Sharp peaks in the XRD confirm high crystalline quality of the samples [Fig. 1(b)]. Detailed structural information was summarized in Table I. Rietveld refinements were carried out with the SHELXL software. ARPES measurements were performed at Beamline 1 of Hiroshima Synchrotron Radiation Center (HSRC), Hiroshima University, Japan, with a VG Scienta R4000 electron analyzer [23]. The photon energy was set at 30 eV. The beam was linearly polarized with its polarization lying in the plane of incidence as well as photoelectron detection plane. The energy and angular resolutions were set at 25 meV and $0.2°$, respectively. Samples were cleaved at 30 K and measured at 20 K, both at vacuum better than 2×10^{-11} mbar. For the magnetotransport measurements, rectangular samples were selected to fabricate into devices to avoid influence of geometry on the results. Electronic contacts were added via patterned mask with photolithography subsequent growth of Ti/Au(10 nm/100 nm) layers. Electrical transport measurements were performed in a physical properties measurement system (PPMS Dynacool, Quantum design). Direct current (dc) magnetization and alternating current (ac) susceptibility measurements were performed in a magnetic property measuring system (MPMS Quantum design).

III. RESULTS AND DISCUSSION

A. Band structure and Fermi surface

Figure 2 shows ARPES spectra of the electronic structure of $EuIn_2As_2$ measured at 20 K, which is above the Néel temperature. Three valence bands α, β, γ (from low to high binding energy) near Fermi level were observed along the $K - \Gamma - K$ direction of the Brillouin zone [Fig. 2(a)]. According to the theoretical calculation [8], $5s$ and $4p$ orbits of In and As respectively dominate the dispersion features near E_F. And all important dispersions reside around the Γ point. We

therefore focus on the certain momentum window around the Γ point as shown in Fig. 2(a). Figure 2(b) shows the constant energy contours of the band structure, with one at E_F and the other 500 meV below E_F. A circular holelike pocket that grows in sizes with increasing binding energy agrees well with Fig. 2(a), and carrier density of pristine $EuIn_2As_2$ can be calculated as 2.2×10^{13} cm^{-2} according to Luttinger theorem with only single band contribution. A zoom-in of Fig. 2(a) enables us to scrutinize the dispersion of the surface band and fit the energy dispersion $\mathbf{E(k)}$ using momentum distribution curve (MDC) cuts. The extracted $\mathbf{E(k)}$ curve is linear with Fermi velocity of 3.7 eV Å (5.7105 m/s) and $k_F = 0.12$ 1/Å [Figs. 2(c) and 2(d)]. In addition, we note that by using the extracted k_F and Fermi velocity, the topmost of the hole pocket can be estimated as about 300 meV above E_F in which resides the topological surface state according to calculation [8]. In consistency with our transport measurements below, the ARPES measurements indicate the pristine $EuIn_2As_2$ is in a metallic state rather than an insulator with E_F lying in the gap. Further tuning the chemical potential by doping or gating the electron would lift the Fermi level close to the predicted topological surface state.

Figure 3 shows the temperature dependent magnetic susceptibility, resistivity $\rho(T)$, magnetoresistivity MR (defined as MR = $[\rho(H) - \rho(0)]/\rho(0)$), and Hall coefficient for the single crystal of $EuIn_2As_2$. Three regions are revealed by different transport behaviors. In the low temperature region
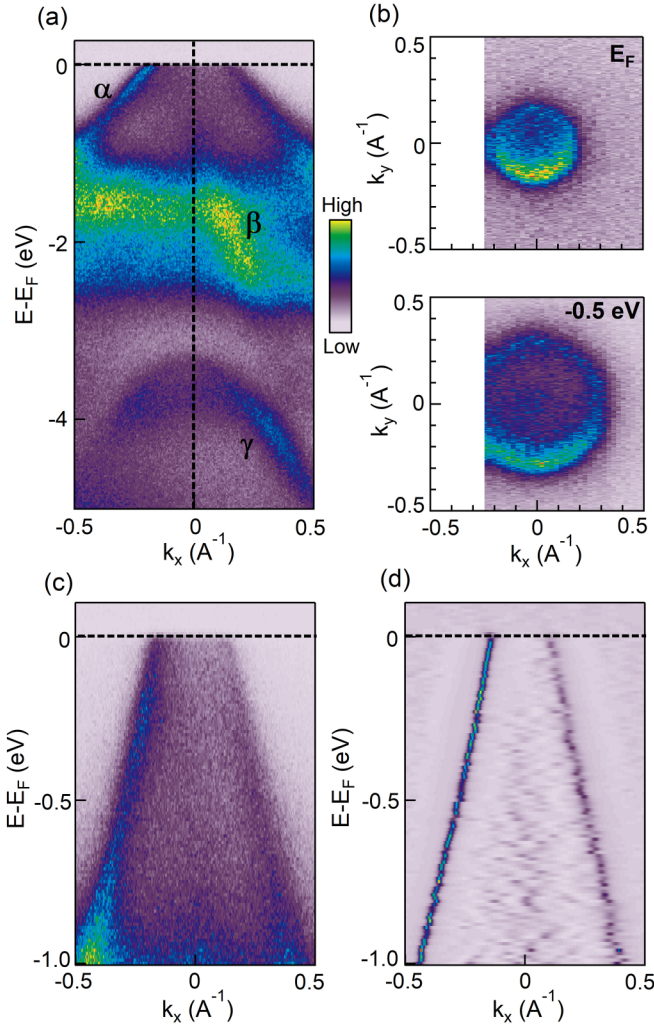
FIG. 2. (a) Valence band structure along the $K - \Gamma - K$ high symmetry direction. Valence bands are labeled from low toward higher binding energy as α, β, and γ. (b) Fermi surface map (top) and constant energy contour at 0.5 eV below the Fermi level. (c) Zoom-in of valence band structure in (a) close to the Fermi level. (d) The corresponding MDC second derivative of (c) to highlight the hole band dispersion.

FIG. 3. (a) Temperature dependent reciprocal of dc magnetic susceptibility of $EuIn_2As_2$ with magnetic field of $H = 0.1$ T applied along the c axis. Deviation from the Curie-Weiss behavior (marked by the red dashed line) is observed below 150 K. (b) Temperature dependent resistivity of $EuIn_2As_2$ with the current along the a axis. Above 150 K the curve is quasilinear. The red dashed line is used to estimate the deviation from the quasilinear behavior below 150 K. Inset: picture of $EuIn_2As_2$ with patterned contacts used for the measurements. (c) Temperature dependence of MR and Hall coefficient at 1 T with $H \parallel c$ are plotted in red and black, respectively. Obvious MR is observed below 150 K and a transition from negative to positive MR occurs around 4 K.

(region I), dc (M/H) magnetic susceptibility reveals the establishment of long range AF order with a transition around 16 K [in Fig. 3(a)] as reported previously [22]. Below this AF transition ($T < T_{AF}$, where T_{AF} is the transition temperature), $\rho(T)$ drops dramatically [in Fig. 3(b)] and negative MR is suppressed [in Fig. 3(c)]. The MR changes its sign to positive at 4 K and reaches up to the largest positive value of 30% at 2 K (the lowest available temperature in our measurments) as shown in Fig. 3(c). This behavior is reminiscent with the observed magnetic phase transition in antiferromagnets due to the appearance of various local magnetic moments [24,25]. In the immediate temperature region (region II), the M/H deviates from Curie Weiss behavior around 150 K linked to the deviation of quasilinear temperature dependence of $\rho(T)$. These results indicate the appearance of short-range magnetic order and the enhancement of magnetic interaction during cooling. In region II, the magnetic order and magnetic

correlation localize the carriers leading to an upturn in $\rho(T)$ curve and a slight increase of the Hall coefficient (less than 3%). In the high temperature region (region III), the M/H curve obeys Curie Weiss law as shown in Fig. 3(a) and $\rho(T)$ exhibits quasilinear temperature dependence [Fig. 3(b)]. In this region, the system behaves as a paramagnetic metal. The MR is negligible and the Hall coefficient keeps a positive value, indicating hole-type carriers [in Fig. 3(c)].

B. Anisotropic magnetic phase diagram

For an AF topological material, the detailed magnetic structure is vital to its topological nature. Theoretical calculations proposed two distinct AF structures with different orientations of the magnetic moments but similar energy for the ground states of $EuIn_2As_2$ [8]. To check these predictions, both dc magnetic susceptibility and magnetotransport measurements were performed in single crystals of $EuIn_2As_2$ with magnetic fields applied along the a axis ($H \parallel a$), b axis ($H \parallel b$), and c axis ($H \parallel c$), respectively, as shown in the inset of Fig. 4(a). The anisotropic temperature dependent magnetization $M(T)$ curves are presented in Fig. 4(a). An obvious upturn is observed with $H \parallel c$ in the low temperature region, while $M(T)$ curves keep decreasing below T_N with both $H \parallel a$ and $H \parallel b$, indicating lower energy of the ground state within
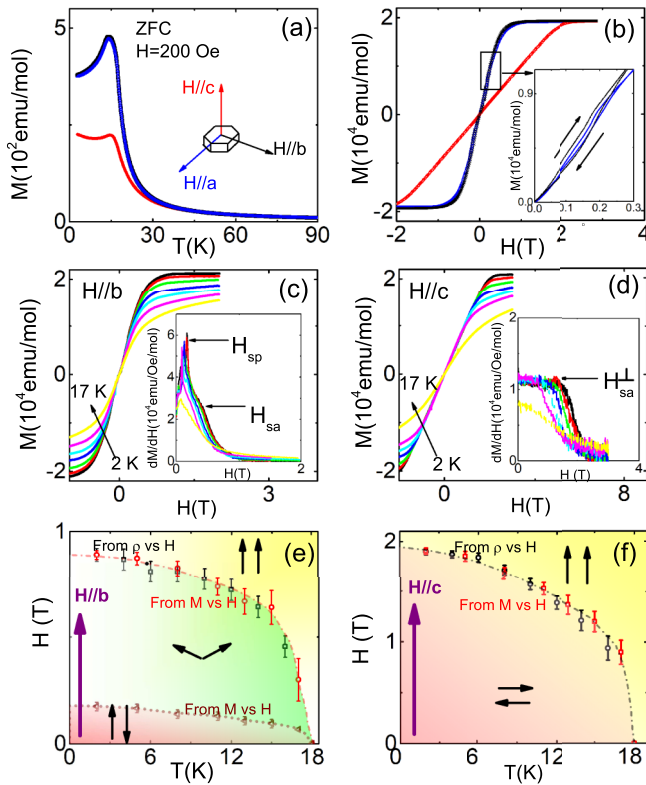
FIG. 4. (a) Temperature magnetization on zero field cooling process (ZFC) for EuIn$_2$As$_2$ with $H = 200$ Oe of $H \parallel a$ (blue line), $H \parallel b$ (black line), and $H \parallel c$ (red line). The inset: the schematic of the geometry of the measured crystal with the applied field. (b) The field dependent magnetization $M(H)$ curves at 2 K with the applied field along three directions as shown in the inset of (a). The $M(H)$ curves in the region marked with a rectangle is zoomed and shown in the inset. A jump of the hysteresis is observed in the $M(H)$ curves, if magnetic field is applied along the a or b axis. (c), (d) $M(H)$ curves with applied field along b and c axis at 2 K, 5 K, 8 K, 11 K, 13 K, 15 K, and 17 K, respectively. The corresponding derivative of $M(H)$ (dM/dH) curves are shown in the insets. We can observe a sharp peak related to magnetic transition with $H \parallel b$. (e), (f) The phase diagrams of EuIn$_2$As$_2$ with $H \parallel b$ and $H \parallel c$, respectively. The purple arrow indicates the direction of applied magnetic field. The black arrows indicate the direction of Eu^{2+} spins. The H_{sa} and $H_{sa}^{\perp}$ acquired from jumps from magnetization measurements and magnetotransport measurements are marked with black and red symbols, respectively. The H_{sp} acquired from the magnetization measurements are marked by blown symbols.

the ab plane [25]. The field dependent magnetization $M(H)$ curves with applied field along different directions exhibit anisotropic behaviors at 2 K as shown in Fig. 4(b). With increasing the applied magnetic field along the a or b axis to a critical value H_{sp}, a small jump in $M(H)$ is observed accompanying a magnetic hysteresis, indicating a magnetic transition [in the inset of Fig. 4(b)]. This abnormal behavior is more clearly identified by a sharp peak in the dM/dH curves as shown in the inset of Fig. 4(c). The magnetization saturates when further increasing the magnetic field to the critical value H_{sa}. As with $H \parallel c$, no additional magnetic transition occurs

besides the saturation (which occurred at $H_{sa}^{\perp}$) [in Figs. 4(b) and 4(d)].

Such anisotropic magnetic behavior can be interpreted within the picture of spin-flop transitions: in a collinear AF system, increasing the applied field to a critical value H_{sp} along, or nearly parallel to, its magnetic easy axis (MEA), the AF sublattice magnetizations M_1 and M_2 rotate abruptly [26]. The staggered magnetization $L = M_1 - M_2$ directs perpendicular to the original MEA instead of aligning itself with the external field direction since the system energy is lower in the former case. This so called spin-flop transition can be detected by a jump in the magnetization loop or a peak in field dependent heat capacity [26,27]. Further increasing the applied magnetic field above H_{sp} will gradually tilt the spin-flopped moments towards the direction of the external magnetic field and finally align the moments of all spins well along the direction of the applied magnetic field at H_{sa}. Thus two transitions will be observed in the case of applied field parallel to MEA. On the other hand, with the applied field perpendicular to the MEA, the AF sublattice spins tilt gradually and are finally well aligned by the external field directly at a critical field $H_{sa}^{\perp}$. As shown in Figs. 4(e) and 4(f), applying the magnetic field along different directions gives rise to the anisotropic magnetic phase diagrams of EuIn$_2$As$_2$. It is noted that the drop in $M(T)$ below T_{AF} and the hysteresis in $M(H)$ with $H \parallel b$ around H_{sp} are larger than those with $H \parallel a$. But the magnetic anisotropy within the ab plane is small and negligible compared to that between in and out of the ab plane. Combining the anisotropic magnetic behavior above, the MEA of EuIn$_2$As$_2$, as well as the direction of ground AF moment, is determined within the ab plane.

C. Multiple magnetic orders

In a simple localized collinear AF system, the magnetization is mainly determined by AF exchange interaction, magnetocrystalline anisotropic energy, and Zeeman energy. Considering the single ion case the Hamiltonian can be written as

$$H = -J \sum \vec{S}_i \cdot \vec{S}_j - D \sum S_{iz}^2 + D \sum S_{jz}^2 - g\mu_B H_0 \left(\sum S_{iz} + \sum S_{jz} \right), \tag{2}$$

where S_i and S_j are the spins at site i and j of the sublattice, H_0 is the applied static magnetic field along the z direction, and J is the exchange constant of the interaction between spins S_i and S_j [28]. The D term represents the uniaxial anisotropy of a single ion and the last term is the usual Zeeman term. With the field applied parallel to the MEA, the molecular field approximation based on a semiclassical model gives critical fields at $T = 0$ K as

$$H_{sp}(0) = [H_A(2H_E - H_A)]^{0.5}, \tag{3}$$

$$H_{sa}(0) = 2H_E - H_A, \tag{4}$$

while, with fields applied perpendicular to the MEA, only the single critical field $H_{sa}^{\perp}(0)$ exists and can be expressed as

$$H_{sa}^{\perp}(0) = 2H_E + H_A, \tag{5}$$

where the $H_E = zJ/g\mu_B$ is the exchange field, $H_A = D/g\mu_B$ is the anisotropy field, and z is the number of nearest neighbors. By extrapolating the experimental $H_{sp}(T)$, $H_{sa}(T)$, and $H_{sa}^{\perp}(T)$ curves to 0 K in Figs. 4(e) and 4(f), the $H_{sp}(0)$ and $H_{sa}(0)$ and $H_{sa}^{\perp}(0)$ are estimated to be 0.18 T, 1.05 T, and 2.1 T, respectively. Employing formulas (3) and (5), we calculate that $H_A = 0.03$ T and $H_E = 0.54$ T. According to formula (4), the calculated $H_{sp}(0) = 0.7$ T is much larger than the experimental value of 0.19 T. The large mismatch may not be understood simply by existence of abnormal spin wave modes [29] but attributed to multiple magnetic orders and interactions.

In our measurements, the upturn in $M(T)$ with $H \parallel c$ suggests weak FM order [25] in region I. By fitting the $M(T)$ curve with the Curie Weiss formula [$M/H = C/(T + \Theta)$, where C is a constant], the calculated positive Curie Weiss temperature $\Theta = 34$ K indicates the ferromagnetic correlation for $EuIn_2As_2$ as well. And the calculated effective moment is $6.93\mu_B$ close to the highest spin state of a single Eu^{2+}, indicating highly localized spins. In the spin-localized AF metal, the appearance of weak FM order can be interpreted as the formation of MP resulting from the large exchange interaction between the conduction electrons and the localized spins [30,31]. For $EuIn_2As_2$, in region I, the long-range AF magnetic order is established widely while the small FM clusters (MP) form locally which would cant the local AF spins. The calculated frustrated parameter $f = 1.9$ (defined as $f = \Theta/T_N$) indicates weak spin frustration as well as favoring the formation of MP [25]. The presence of FM order broadens the spin-flop transition (compared to the sharp one in $EuSn_2As_2$ [32,33]) and leads to the failure of the simple AF model. In region II, the observed derivation of Curie Weiss law for $\chi(T)$ suggests the MP can persist with the absence of long-range AF order to the higher temperature region. The presence of multiple magnetic orders and correlations in $EuIn_2As_2$ is also in accordance with our magnetotransport characterizations below.

As shown in Fig. 5(a) the MR for $EuIn_2As_2$ exhibits non-monotone evolutions with both $H \parallel b$ and $H \parallel c$ relating to the detailed magnetic states. In region I, the observed positive MR in the low field region increases with rising applied field to the maximum value around the saturation fields H_{sa} and $H_{sa}^{\perp}$. With further increase of the magnetic field, the MR decreases and eventually becomes negative at higher fields. The maximum of field dependent magnetoresitivity [MR(H)] moves towards lower fields, as well as reduces the intensity, with increasing the temperature, and finally disappears at T_N. The MR(H) curves exhibit a kink for $H \parallel b$ near H_{sp} while varying smoothly below the $H_{sa}^{\perp}$ for $H \parallel c$ as shown in Fig. 5(b), in accordance with the observed anisotropic magnetic behavior above. In this region, the magnetotransport behavior can be understood by a picture of the crossing from weak localization to weak antilocalization due to the competition of AF and FM orders [25]. The long-range AF order localizes the carriers leading to the increasing MR at low magnetic fields. At high magnetic fields, the AF spins are flipped and the MP increases in size, giving rise to the decrease of hopping energy, thus resulting in the negative MR.

In region II, only negative MR is observed due to the absence of long-range AF order. The spin scattering due to
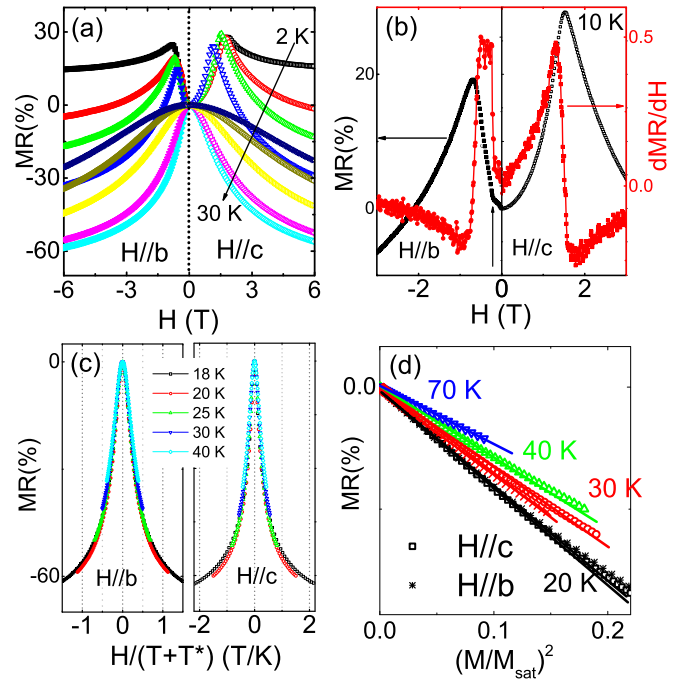
FIG. 5. (a) MR for $EuIn_2As_2$ at 2 K, 6 K, 10 K, 14 K, 16 K, 18 K, 20 K, and 30 K with $H \parallel b$ (left panel) and $H \parallel c$ (right panel), respectively. (b) Zoomed MR and dM/dH at 10 K with $H \parallel b$ and $H \parallel c$, respectively. (c) Scaled MR at 18 K, 20 K, 25 K, 30 K, and 35 K with $H \parallel b$ and $H \parallel c$, respectively. (d) The MR fitted by ML model at 20 K, 30 K, 40 K, and 70 K with $H \parallel c$ and the MR fitted by ML model at 20 K and 30 K with $H \parallel b$.

localized magnetic moments will be suppressed by aligning local moments giving rise to more itinerant carriers [22]. By using the Bethe-ansatz method [34], the MR(H) curves at various temperatures can be scaled onto a single curve with the relation

$$\text{MR}(H) = f\left(\frac{H}{T + T^*}\right), \quad (6)$$

as shown in Fig. 5(c), where T^* is a characteristic temperature relating to the magnetic order. For $H \parallel b$ and $H \parallel c$, the T^*'s are acquired to be -14.5 K and -14 K, respectively. The negative value indicates the presence of FM correlations or FM orders [34] in $EuIn_2As_2$ agreeable with the MP scenario. In this region, the bound MP and crystal field of Eu ion trap the carriers, leading to the negative $d\rho/dT$ and the large upturn of $\rho(T)$ above T_N.

Within the argument of the Majumdar-Littlewood (ML) model [30], the MR is related to the scaled magnetization M/M_{sat} by the formula

$$|[\rho(H) - \rho(0)]/\rho(0)| \approx (1/2k_f\xi_0)^2 (M/M_{sat})^2, \quad (7)$$

where ξ_0 is the correlation length. Figure 5(d) shows the MR curves fitted by the ML formula suggesting the presence of MP above T_{AF}. The calculated correlation length ξ_0 increases with decreasing temperature ranging from 3.4 Å (at 70 K) to 5.2 Å (at 20 K). The $n\xi_0^3$ (n is the carrier density) for $EuIn_2As_2$ is calculated as $n\xi_0^3 = 0.051$. This value is much smaller than 1 in accordance with the formation of MP. Since the obvious chemical inhomogeneity and crystal defect are
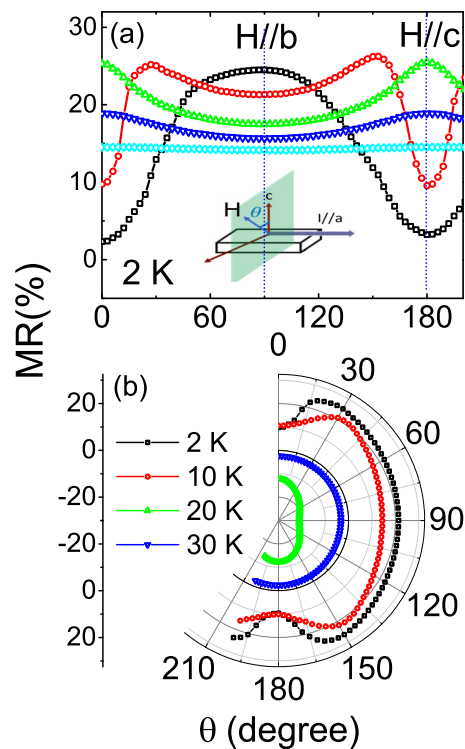
FIG. 6. (a) AMR at 2 K with $H = 0.5$ T, 1 T, 2 T, 3 T, and 6 T. Inset: schematic of the configuration of the rotating sample. (b) Angular dependence of MR at 2 K, 10 K, 20 K, and 30 K with $H = 1$ T.

not observed by SEM and single crystal diffraction measurements, the bound MP may originate from a small amount of Eu^{3+} valence or small impurities with subnanosize, which needs further investigation later.

The angular dependent magnetoresistivity (AMR) curves are shown in Figs. 6(a) and 6(b) with the measurement configuration shown in the inset of Fig. 6(a). The current flows along the a axis and the magnetic field is applied and rotates within a plane perpendicular to the current. Magnetic field-induced changes in the AMR symmetry are observed. At 2 K, a twofold symmetric MR is observed with a maximum value in the direction of $H \parallel b$ ($H = 0.5$ T). With increase of the applied field, MR exhibits a maximum for the direction of $H \parallel c$ ($H = 2$ T) due to the canted spins and MP. With further increase of the field, the MR becomes isotropic as

shown in Fig. 6(a) indicating the saturated magnetization. With increase of the temperature, the AMR exhibits a similar symmetry evolving with $H = 1$ T and changes the value from positive to negative as shown in Fig. 6(b). The field-induced or temperature-induced changes in the AMR indicate that the magnetic states can be tuned by external conditions. For $EuIn_2As_2$, the multiple magnetic orders, such as long-range AF order and short-range FM order, are vital to its topological nature. The tunable magnetic states enlighten us to explore the possible topological states or topological transitions by controlling external conditions. For example, the applied magnetic field controls both the spin canting as well as Zeeman splitting leading to the movement of Weyl points accompanying the magnetic field-induced changes of the AMR in topological materials such as $ZrTe_5$ and $EuTiO_3$ [35,36].

IV. CONCLUSION

The electronic structure and transport properties are systematically studied for the ATI candidate $EuIn_2As_2$. Hole-type Fermi pockets are revealed and the linear energy dispersion near the Fermi level agrees with the proposed topological state around the Γ point. The anisotropic magnetic phase diagrams and magnetotransport properties indicate in-plane AF moments of the ground state. The short-range FM orders are suggested by magnetization and magnetotransport measurements, which can be understood by the picture of MP. The presence of multiple magnetic orders and interactions in $EuIn_2As_2$ is important to understand the topological nature or even tune the topological states in $EuIn_2As_2$.

[1] X.-L. Qi, T. L. Hughes, and S.-C. Zhang, Phys. Rev. B **78**, 195424 (2008).

[2] R. Li, J. Wang, X. L. Qi, and S. C. Zhang, Nat. Phys. **6**, 284 (2010).

[3] F. Wilczek, Phys. Rev. Lett. **58**, 1799 (1987).

[4] D. Zhang, M. Shi, T. Zhu, D. Xing, H. Zhang, and J. Wang, Phys. Rev. Lett. **122**, 206401 (2019).

[5] S. Chowdhury, K. F. Garrity, and F. Tavazza, npj Comput. Mater. **5**, 33 (2019).

[6] A. Zeugner, F. Nietschke, A. U. B. Wolter, S. Gaß, R. C. Vidal, T. R. F. Peixoto, D. Pohl, C. Damm, A. Lubk, R. Hentrich, S. K. Moser, C. Fornari, C. H. Min, S. Schatz, K. Kißner,

M. Unzelmann, M. Kaiser, F. Scaravaggi, B. Rellinghaus, K. Nielsch, C. Hess, B. Büchner, F. Reinert, H. Bentmann, O. Oeckler, T. Doert, M. Ruck, and A. Isaeva, Chem. Mater. **31**, 2795 (2019).

[7] M. M. Otrokov, I. P. Rusinov, M. Blanco-Rey, M. Hoffmann, A. Yu. Vyazovskaya, S. V. Eremeev, A. Ernst, P. M. Echenique, A. Arnau, and E. V. Chulkov, Phys. Rev. Lett. **122**, 107202 (2019).

[8] Y. Xu, Z. Song, Z. Wang, H. Weng, and X. Dai, Phys. Rev. Lett. **122**, 256402 (2019).

[9] J. Li, Y. Li, S. Du, Z. Wang, B.-L. Gu, S.-C. Zhang, K. He, W. Duan, and Y. Xu, Sci. Adv. **5**, eaaw5685 (2019).

[10] J.-Q. Yan, Q. Zhang, T. Heitmann, Z. Huang, K. Y. Chen, J.-G. Cheng, W. Wu, D. Vaknin, B. C. Sales, and R. J. McQueeney, Phys. Rev. Materials **3**, 064202 (2019).

[11] Y. Deng, Y. Yu, M. Z. Shi, J. Wang, X. H. Chen, and Y. Zhang, science **367**, 895 (2020).

[12] J. Ge, Y. Liu, J. Li, H. Li, T. Luo, Y. Wu, Y. Xu, and J. Wang, arXiv:1907.09947.

[13] C. Liu, Y. Wang, H. Li, Y. Wu, Y. Li, J. Li, K. He, Y. Xu, J. Zhang, and Y. Wang, Nat. Mater. **19**, 522 (2020).

[14] B. Chen, F. Fei, D. Zhang, B. Zhang, W. Liu, S. Zhang, P. Wang, B. Wei, Y. Zhang, Z. Zuo, J. Guo, Q. Liu, Z. Wang, X. Wu, J. Zong, X. Xie, W. Chen, Z. Sun, D. Shen, S. Wang, Y. Zhang, M. Zhang, X. Wang, F. Song, H. Zhang, and B. Wang, Nat. Commun. **10**, 4469 (2019).

[15] B. Li, J.-Q. Yan, D. M. Pajerowski, E. Gordon, A. M. Nedić, Y. Sizyuk, L. Ke, P. P. Orth, D. Vaknin, and R. J. McQueeney, Phys. Rev. Lett. **124**, 167204 (2020).

[16] R. C. Vidal, H. Bentmann, T. R. F. Peixoto, A. Zeugner, S. Moser, C. H. Min, S. Schatz, K. Kissner, M. Unzelmann, C. I. Fornari, H. B. Vasili, M. Valvidares, K. Sakamoto, D. Mondal, J. Fujii, I. Vobornik, S. Jung, C. Cacho, T. K. Kim, R. J. Koch, C. Jozwiak, A. Bostwick, J. D. Denlinger, E. Rotenberg, J. Buck, M. Hoesch, F. Diekmann, S. Rohlf, M. Kallane, K. Rossnagel, M. M. Otrokov, E. V. Chulkov, M. Ruck, A. Isaeva, and F. Reinert, Phys. Rev. B **100**, 121104(R) (2019).

[17] Y. Gong, J. Guo, J. Li, K. Zhu, M. Liao, X. Liu, Q. Zhang, L. Gu, L. Tang, X. Feng, D. Zhang, W. Li, C. Song, L. Wang, P. Yu, X. Chen, Y. Wang, H. Yao, W. Duan, Y. Xu, S.-C. Zhang, X. Ma, Q.-K. Xue, and K. He, Chin. Phys. Lett. **36**, 076801 (2019).

[18] H. Li, S. Liu, C. Liu, J. Zhang, Y. Xu, R. Yu, Y. Wu, Y. Zhang, and S. Fan, Phys. Chem. Chem. Phys. **22**, 556 (2020).

[19] Y. J. Chen, L. X. Xu, J. H. Li, Y. W. Li, C. F. Zhang, H. Li, Y. Wu, A. J. Liang, C. Chen, S. W. Jung, C. Cacho, H. Y. Wang, Y. H. Mao, S. Liu, M. X. Wang, Y. F. Guo, Y. Xu, Z. K. Liu, L. X. Yang, and Y. L. Chen, Phys. Rev. X **9**, 041040 (2019).

[20] P. Swatek, Y. Wu, L.-L. Wang, K. Lee, B. Schrunk, J. Yan, and A. Kaminski, Phys. Rev. B **101**, 161109(R) (2020).

[21] Y.-J. Hao, P. Liu, Y. Feng, X.-M. Ma, E. F. Schwier, M. Arita, S. Kumar, C. Hu, R. Lu, M. Zeng, Y. Wang, Z. Hao, H. Sun,

[K. Zhang, J. Mei, N. Ni, L. Wu, K. Shimada, C. Chen, Q. Liu, and C. Liu, Phys. Rev. X **9**, 041038 (2019).

[22] A. M. Goforth, P. Klavins, J. C. Fettinger, and S. M. Kauzlarich, Inorg. Chem. **47**, 11048 (2008).

[23] H. Iwasawa, K. Shimada, E. F. Schwier, M. Zheng, Y. Kojima, H. Hayashi, J. Jiang, M. Higashiguchi, Y. Aiura, H. Namatame, and M. Taniguchi, J. Synchrotron Rad. **24**, 836 (2017).

[24] P. F. S. Rosa, C. Adriano, T. M. Garitezi, R. A. Ribeiro, Z. Fisk, and P. G. Pagliuso, Phys. Rev. B **86**, 094408 (2012).

[25] W. Shon, J.-S. Rhyee, Y. Jin, and S.-J. Kim, Phys. Rev. B **100**, 024433 (2019).

[26] Y. Shapira and S. Foner, Phys. Rev. B **1**, 3083 (1970).

[27] H.-F. Li, npj Comput. Mater. **2**, 16032 (2016).

[28] C. C. Becerra, N. F. Oliveira, Jr., A. Paduan-Filho, W. Figueiredo, and M. V. P. Souza, Phys. Rev. B **38**, 6887 (1988).

[29] F. L. A. Machado, P. R. T. Ribeiro, J. Holanda, R. L. Rodriguez-Suarez, A. Azevedo, and S. M. Rezende, Phys. Rev. B **95**, 104418 (2017).

[30] P. Majumdar and P. B. Littlewood, Nature (London) **395**, 479 (1998).

[31] M. Pohlit, S. Rößler, Y. Ohno, H. Ohno, S. von Molnàr, Z. Fisk, J. Müller, and S. Wirth, Phys. Rev. Lett. **120**, 257201 (2018).

[32] H. Li, S. Gao, S. Duan, Y. Xu, K. Zhu, S. Tian, W. Shan, Z. Rao, J. Huang, J. Li, Z.-T. Liu, W.-L. Liu, Y.-B. Huang, Y.-L. Li, Y. Liu, G.-B. Zhang, H.-C. Lei, Y.-G. Shi, W.-T. Zhang, H.-M. Weng, T. Qian, and H. Ding, Phys. Rev. X **9**, 041039 (2019).

[33] X. Gui, I. Pletikosic, H. Cao, H.-J. Tien, X. Xu, R. Zhong, G. Wang, T.-R. Chang, S. Jia, T. Valla, W. Xie, and R. J. Cava, arXiv:1903.03888.

[34] P. Schlottmann, Phys. Rep. **181**, 1 (1989).

[35] G. Zheng, X. Zhu, Y. Liu, J. Lu, W. Ning, H. Zhang, W. Gao, Y. Han, J. Yang, H. Du, K. Yang, Y. Zhang, and M. Tian, Phys. Rev. B **96**, 121401(R) (2017).

[36] K. Ahadi, X. Lu, S. Salmani-Rezaie, P. B. Marshall, J. M. Rondinelli, and S. Stemmer, Phys. Rev. B **99**, 041106(R) (2019).]

Correction: The omission of a support statement in the Acknowledgment section has been fixed.